Available online at www.eccomasproceedia.org
Eccomas Proceedia UNCECOMP (2023) 599-620

ECCOMAS
Proceedia

UNCECOMP 2023
5th ECCOMAS Thematic Conference on
Uncertainty Quantification in Computational Science and Engineering
M. Papadrakakis, V. Papadopoulos, G. Stefanou (eds.)
Athens, Greece, 12-14 June 2023

QUANTIFYING UNCERTAINTIES IN NUMERICAL PREDICTIONS OF DYNAMIC CAVITATION

Erdinc KARA[1,2], Artur K. Lidtke[2], Bülent Düz[2], Douwe Rijpkema[2], and O. Kemal Kinaci[1]

[1]Istanbul Technical University
Istanbul, Turkey
e-mail: {karae15, kinacio}@itu.edu.tr

[2] Maritime Research Institute Netherlands
Wageningen, Netherlands
e-mail: {A.Lidtke, B.Duz, D.R.Rijpkema}@marin.nl

Abstract. *Cavitation on marine propellers is an important issue due to its negative effects on many aspects of their operation. Therefore, accurate prediction of cavitation is important to ensure better propeller design. Estimating the cavitation behavior numerically is a difficult task due to the high computational cost of simulations and various numerical uncertainties. This study is carried out in order to estimate the parameter and discretization uncertainties and combine them into a single value using an example 2D foil as the test case. Angle of attack and the cavitation number are selected as input parameters and their influence on force coefficients and sheet cavity properties is studied. Sobol indices are also obtained to measure the relative importance of the input and discretization uncertainties. It is seen that uncertainty in the angle of attack has a much greater influence on the force coefficients than the uncertainty in the cavitation number or grid discretization uncertainty. On the other hand, the cavitation number uncertainty is dominant over the grid and angle of attack uncertainties for the length and volume of the cavity sheet. According to the results obtained, applying only the grid refinement studies is not sufficient for the estimation of the numerical uncertainties for this kind of CFD problems. It is proposed that assessing both parameter and discretization uncertainties for the presented and other similar applications with epistemic uncertainties should be applied more often.*

Keywords: Parameter uncertainty, Discretization uncertainty, Uncertainty Quantification, Sobol indices, CFD, Cavitation

ISSN:2623-3339
Peer-review under responsibility of the organizing committee of UNCECOMP 2023.
doi: 10.7712/120223.10361.19618

1 INTRODUCTION

The presence of cavitation in marine propellers is a critical problem that can drastically reduce propeller efficiency whilst causing erosion of the blade surface and increasing the generated noise and vibrations. Even though it is an important phenomenon that needs to be considered at the early design stages of a ship, prediction of propeller cavitation behaviour numerically remains a challenging task, mainly due to high computational cost and deficiencies of the available numerical models. Additionally, uncertainties associated with the choice of boundary condition values, various modelling constants, grid density, and time step size are still far from understood.

The main aim of this study is to address these issues by applying uncertainty quantification techniques to CFD simulations of cavitation using MARIN's in-house code, ReFRESCO[1]. Cavitation behaviour on a 2D hydrofoil is investigated. The chosen test case is the NACA 66 foil studied experimentally by [1] and others. The popularity of this test case stems from its relevance to marine propeller design and the wide availability of experimental and reference numerical data. An example cavitating flow for this foil is depicted in Figure 1. A characteristic condition corresponding to steady sheet cavitation has been selected using the experimental data available and a series of simulations around that point have been carried out to sample the sensitivity of the CFD solution. Subsequently, uncertainty quantification (UQ) has been applied to the results in order to study the effect of input parameters and grid density on the cavitation behaviour. This step took after the methodology previously developed by [2] and applied to non-cavitating propellers and flat plates at transitional Reynolds numbers.

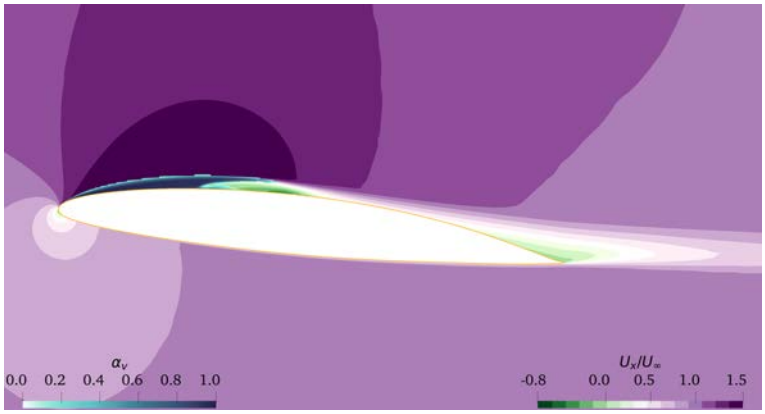

Figure 1: Overview of the vapour volume fraction (α_v) and streamwise velocity around the considered NACA 66 foil. Conditions mimic those of the experimental study of [1] at 6 degrees angle of attack.

2 METHODOLOGY

2.1 Uncertainty Quantification in CFD Applications

Uncertainties can be classified under two headings as aleatoric (also called stochastic uncertainty) and epistemic uncertainties. The former are the random variable uncertainties that arise due to the nature of the process. Epistemic uncertainty, also known as systematic uncertainty, arises from things that are known in principle but cannot be fully known in practice, for reasons such as not having enough knowledge or data at any stage, neglecting certain effects,

[1] https://www.marin.nl/en/facilities-and-tools/software/refresco

sensitivity limitations of measurement tools, etc. [3–5]. While aleatory uncertainties cannot be reduced with the further knowledge, more data and knowledge would allows for more accurate and more precise epistemic uncertainty estimation[6]. In the context of UQ applications to CFD simulations, uncertainties related to the input parameters such as material features, or initial-boundary conditions are referred to as aleatoric uncertainties since they have inherent randomness in some cases; uncertainties related to the parameters not known precisely are referred as epistemic uncertainty [2]. Uncertainties encountered in the input parameters mean that there are also uncertainties in the output data obtained as a result of the simulations. Therefore, UQ analysis is applied to determine and estimate the uncertainties that have an effect on the outputs by studying and quantifying the effect of the uncertain input variables. Hirsch and Dinescu [7] implemented the intrusive polynomial chaos methodology to simulations of the transonic flow in the NASA Rotor 37 axial compressor. Phillips and Roy [8] presented a new uncertainty estimator for CFD applications based on Richardson extrapolation. It utilizes global order of accuracy and assorted metrics to calibrate and appraise the uncertainty estimator. Cuneo et al. [9] applied and assessed four uncertainty quantification methods, namely Monte Carlo, Polynomial Chaos, Mid-range Approximation, and a combined Monte Carlo and Polynomial Chaos method, to multiple analytical test functions and engineering test cases. Although there has been a substantial amount of research effort dedicated to making the Stochastic Galerkin method easier to use, doing so still poses challenges. Researchers choose the non-intrusive approaches due to not only using a computational model is easy and adventageous but also Galerkin method has the possibility of expeditiously increase in the computational cost with the number of random dimensions [2, 10]. However, in practice, the large number of samples typically required in the sampling-based approaches can greatly increase the computational cost of CFD simulations. In the present study, the non-intrusive approach is coupled with a surrogate model of the CFD solution in order to overcome this issue.

2.2 Design of Experiments (DoE)

Design of Experiment (DoE) refers to statistical approaches used to sample a function, be it a set of CFD solutions or an explicit mathematical function, in a methodical and efficient manner [11]. Many categories of such approaches exist, including Monte Carlo Sampling [12, 13], Quasi-Monte Carlo Sampling [13, 14], Latin Hypercube Sampling (LHS) [14–17], and Hammersley Sequence Sampling (HSS)[18, 19].

In this study, Latin Hybercube Sampling (LHS) is selected as the DoE because of it might provide more accurate mean values of the function than Monte Carlo sampling [2]. This approach is employed in order to distribute the CFD simulations in the parameter space in a way that will achieve a quality fit of the response surface while minimising the total computational effort. Sampling model and the distribution of the input parameters used in this study is shown in Figure 2.

Overall 25 sample points have been used, of which 20 are distributed using LHS and 5 are placed in the corners and centre of the domain. This approach is therefore referred to as a combined shell and LHS distribution.

Leroux [1] studied the flow past a NACA 66 foil and observed the partial cavitation growth and/destabilization cycles at angles of attack of 6 and 7 degrees for a range of cavitation numbers. One of the reported experimentally studied conditions has been chosen as the basis of the present study. In an associated study using a similar experimental set up, the authors quote the measurement uncertainty of the cavitation number to be 3%, the angle of attack approximately 3.5%, and inflow velocity 2% [1]. These values have been used in order to sample the

CFD solution, assuming the angle of attack and cavitation number to be the two independent input parameters. Uncertainty of the inflow velocity, and hence Reynolds number, has not been taken into account given the known and relatively small dependence of sheet cavitation extents on this parameter at sufficiently high Reynolds numbers [20]. In order to remain conservative, a slightly larger extent of the sampling domain of 5% has been decided on.

According to CFD results conducted with the first sampling, it is observed that some cases -because they are very close to the unstable partial cavitation region- exhibit unstable properties (an unstable structure, especially in cavitation size and volume, since periodic sheet cavity occurs). Therefore, for a more stable cavitation to occur, a different validation data ($\sigma = 1.5494$) in Leroux's study, is accepted as the new cavitation number.

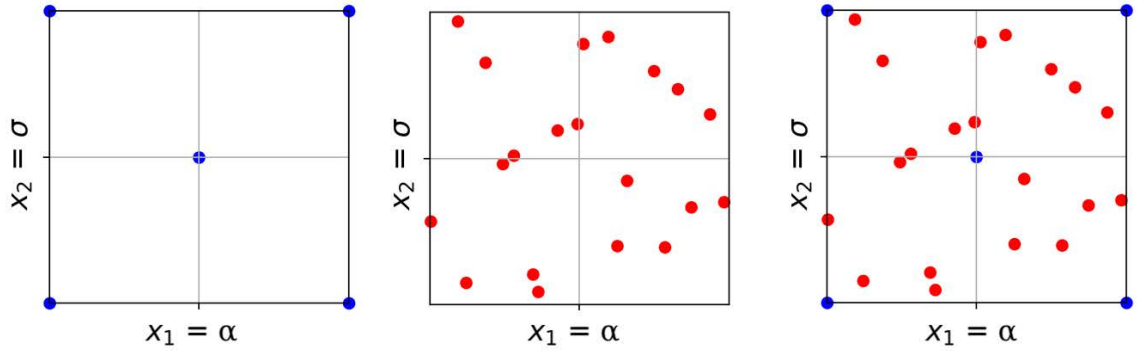

Figure 2: Sampling created for two uncertain input parameters which are (α) and (σ), by applying Shell distribution (left); Latin Hybercube Sampling distribution (center), and combined LHS + Shell distribution (right).

2.3 Surrogate Modeling

A surrogate model (also called as meta-model or response surface approximation) is a function which approximates the results of an an experiment or a simulation and is computationally less expensive than approach originally used to produce the data. In this approach, instead of sampling the large number of samples needed for UQ analysis, a suitable surface is defined with the data generated with a smaller number of samples. Then, the values of the desired points on the surface can be obtained by using the response surface equation. Sobester et al. [21] outlines the modeling steps that need to be followed in order to create a surrogate model. These are arranging the data and selecting an approach for modeling, forecasting and running of the parameters, and testing the model. Different types of surrogate model approaches such as Polynomial Chaos Expansios (PCE) [22–24], Kriging model (also known as a Gaussian process model) [25–27], Multivariate Adaptive Regression Splines (MARS) [28–31], Radial Basis Functions (RBF) [25, 32, 33], Artificial Neural Networks (ANN) [25, 26, 34] , Moving Least Squares (MLS) [35–37], and multifidelity models [25, 38] are discussed and compared in many studies in various fields. However, the mentioned methods indirectly require that the related output parameters have to vary smoothly according to uncertain input parameters. In cases where the output parameters are not properly distributed according to the input parameters, that is, a smooth response surface is not guaranteed, these methods may significantly reduce the accuracy. Some studies have also been carried out to develop techniques for such non-smooth responses. Zhang et al. [39] developed the Adaptive Hybrid Functions (AHF) which is a new high accuracy hybrid surrogate modeling technique that combines the favorable characteristics

of several surrogate models in order to model non-smooth functions. Methods are presented by Shimoyamaet al. [40] in order to obtain the polynomial chaos coefficients for modeling the non-smooth responses. A two stage approach where the distinct behaviors are first localized and categorized and thereafter approximations made locally is studied by Moustapha et al. [41] for non-smooth functions encountered in engineering problems. Similar studies for non-smooth response functions have been investigated in [42–44]. In this study involving a steady-sheet cavity flow, it is expected that to have simple, smooth response surfaces to be formed for the desired output parameters (lift coefficient C_L, drag coefficient C_D, cavitation length V_{cav}, and cavity volume V_{cav}) according to the determined inputs (angle of attack α, and cavitation number σ) will be smooth. Therefore, surrogate model based on piecewise linear approximation, as proposed by [43] is used. In this approach, linear interpolations are performed between the nearest three points of the sampling. Being more consistent due to their lower-order nature compared to polynomial-based approximations, is the advantage that makes this approach stand out. More detailed review on piecewise linear methods is presented in [44] showing the use of this method in a wide variety of applications. An example response surface and the surrogate model created according to the input parameters distribution and their response outputs $z = f(x, y)$ calculated from the CFD simulations is shown in Figure 3.

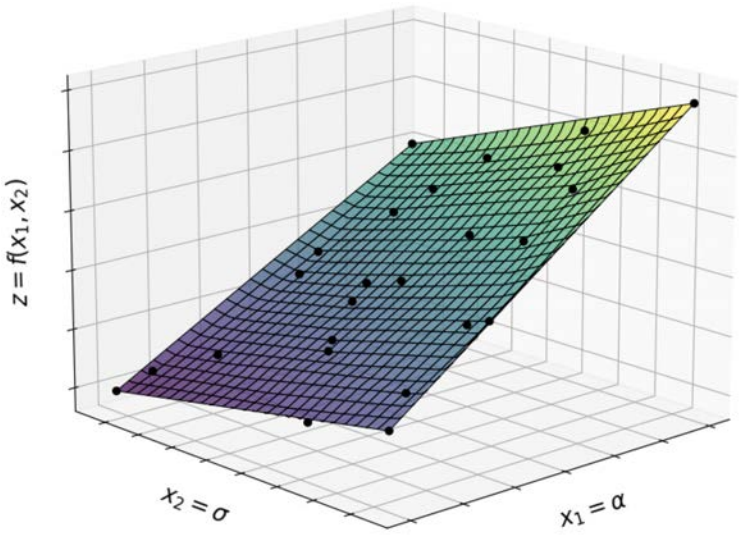

Figure 3: Schematic representation of the used surrogate model of drag coefficient (C_D): True response and sampled points (marked in black dots) from CFD results.

2.4 Global Sensitivity Analysis and the Sobol Method

In global sensitivity analysis, unique parameter pairs are created by assigning different values to the input parameters in the system simultaneously within a certain domain. Thus, it is possible to see the relative effects of the input parameters on the output parameters, the interactions of the input parameters, as well as the effects of these interactions on the results. In summary, sensitivity analysis is an approach used to determine how much influence a given input parameter has on the behavior of the system, or which parameters interact with each other and how much this interaction affects the results [45].

Sobol [46] introduced an approach that would later be referred to as the Sobol's method which makes it possible to compute the total contribution of each individual input parameters

and their interactions to the output's variance [45, 47]. In the Sobol's method, it is aimed to determine how much of the change in the output parameters of the model is either due to the change of a single parameter individually or the interaction between different input parameters. The selection of the input parameters and the reasons for the change are not emphasized, only the extent to which the changes of the input parameters have an effect on the output parameters. The flow chart and the steps of the Sobol sensitivity analysis are given in Figure 4. The complete process consists of the preparation step to the Sobol analysis, referred to as pre-Sobol analysis, and the main Sobol sensitivity analysis step. Sobol sensitivity analysis can be applied by following four steps which are generating the parameter sets, running the simulations for generated input parameter combinations and obtaining the model output data, calculating the Sobol indices, and analyzing the total, first, second and higher-order Sobol sensitivity indices [45].

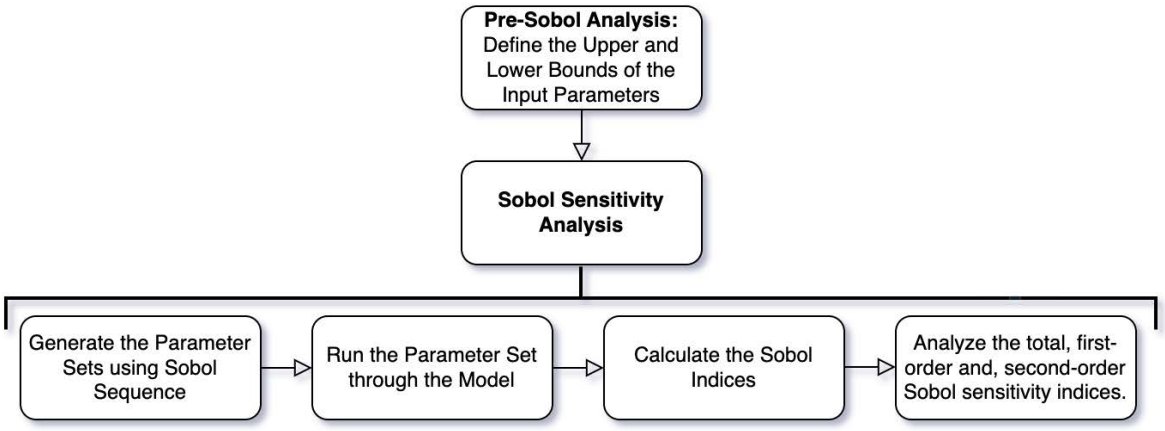

Figure 4: The flow chart and the steps of the Sobol sensitivity analysis.

Consider $\mathbf{X} = (X_1, X_2, ..., X_N)$ as the input parameters and $Y = f(X_1, X_2, ..., X_N)$, as an output of the model, in which N represents the number of inputs. Indices which measure the contribution of the uncertain input parameters individually to the output Y are the first-order Sobol indices (S_i), defined as:

$$S_i = \frac{V_{X_i}\left(E_{\mathbf{X}_{\sim i}}(Y|X_i)\right)}{V(Y)} \tag{1}$$

where $V(Y)$ indicates the variance of Y and $E_{\mathbf{X}_{\sim i}}$ the expectation taken over all X in $\mathbf{X}$, except X_i. S_i is a number between 0 and 1 where a high value indicates an important variable. Higher order indices, e.g. second-order (S_{i+j}), measure the contribution of the interaction between the inputs, which results in:

$$\sum_{i=1}^{N} S_i + \sum_{1\leq i\leq j}^{N} S_{i+j} + ... + S_{i+j+k...+N} = 1 \tag{2}$$

For three input parameters, as we are considering in this study, this leads to:

$$S_1 + S_2 + S_3 + S_{1+2} + S_{1+3} + S_{2+3} + S_{1+2+3} = 1 \tag{3}$$

Total-order index (ST) considers the contribution of all the first- and high-order indices and sum of all ST equals to 1 [48–50], defined as:

$$ST_i = \frac{E_{\mathbf{X}_{\sim i}}\left(V_{X_i}(Y|\mathbf{X}_{\sim i})\right)}{V(Y)} \tag{4}$$

which leads to the following total-order indices for three input parameters to:

$$\begin{aligned} ST_1 &= S_1 + S_{1+2} + S_{1+3} + S_{1+2+3} \\ ST_2 &= S_2 + S_{1+2} + S_{2+3} + S_{1+2+3} \\ ST_3 &= S_3 + S_{1+3} + S_{2+3} + S_{1+2+3} \end{aligned} \tag{5}$$

More information about the Sobol method and Sobol indices is given in [50, 51]. In the context of this study, the Sobol analysis is carried out by using the Sensitivity Analysis Library (SALib) implemented in Python [52].

2.5 Output variables and their statistics

An empirical probability distribution (EDF or also called Empirical Cumulative Distribution Function, ECDF) is used when the data sample cannot be fitted to any known probability distribution function or cannot be obtained by data transformations or parameterization of the distribution function. In other words, the empirical CDF is built from an actual data set in contrast to the CDF which is a theoretical construct. In this study, the empirical distribution functions (EDF) is evaluated from the input parameter distribution in order to estimate the cumulative distribution function (CDF) of the output variables. Given N_i samples x_i, the EDF for the value t is numerically calculated by:

$$EDF(t) = \frac{1}{N_i}\sum_{n=1}^{N_i} H(t - x_i[n]) \rightarrow CDF(t) \tag{6}$$

where $H(x)$ is the Heaviside function. The empirical CDF usually approximates the CDF quite well, especially for large samples. If the number of samples N_i tends to infinity, EDF converges to the CDF for every value of t [53]. Considering p and $\bar{p}$ to be two probability levels, the confidence interval between them can be calculated by taking the inverse of the cumulative distribution functions (also known as the quantile function). Here, confidence level is taken to be 95% as it is generally adopted in the literature [2]. A more stringent criterion could be selected in safety-critical applications, for instance. The length of the error bars is calculated as:

$$CI_{length} = CDF^{-1}(0.975) - CDF^{-1}(0.025). \tag{7}$$

2.6 Combined Grid and Parameter Uncertainty

Combination of parameter and discretization uncertainty processes is carried out by applying the method proposed by Katsuno et. al. [2]. In this context, uncertainty due to discretization is included in the Sobol analysis as an extra input variable. Here, this is referred to as *xgrid*, and represents the percentile of the discretization uncertainty. Simulations of the 25 selected conditions are run for each grid refinement level and response surfaces are obtained for each grid. This is illustrated in Figure 5.

There are 8 surrogate models for the 8 different meshes (G1 is the coarsest grid and G8 is the finest grid), each of them created by the results of CFD simulations. For an input parameter

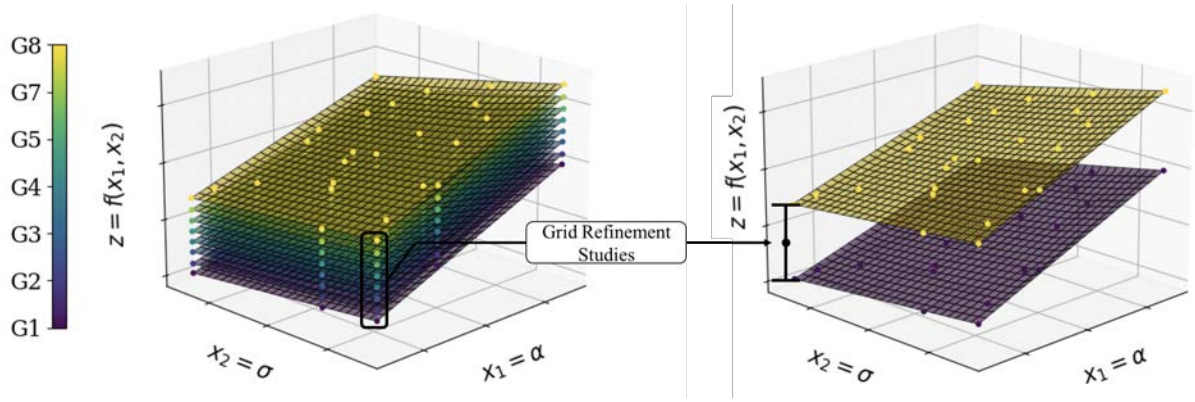

Figure 5: Surrogate models for each grid refinement levels. G1 represents the coarsest grid, G8 represents the finest grid. Response surfaces are created on each grid first and then combined in the final part of the analysis.

couple (x_1, x_2), there are 8 different output parameter values of $z = z(x_1, x_2)$. These are used in the numerical uncertainty estimation method of Eca and Hoekstra [54], which yields a least-squares fit to the simulated data as a function of grid refinement level, as well as the confidence interval.

After discretization uncertainty x_{grid} is defined as the third input uncertainty, the probability density function of it is defined. Due to its definition, the PDF of x_{grid} is always non-negative and its integral over the entire space is equal to one. These definitions are given in Eqs. (8a) and (8b), assuming the discretization PDF is presented as h(x).

$$h(x) \geq 0 \tag{8a}$$

$$\int_{-\infty}^{+\infty} h(x)dx = 1 \tag{8b}$$

$$\int_{y_b}^{y_t} h(x)dx = 0.95 \tag{8c}$$

$$\int_{-\infty}^{\phi_1} h(x)dx = \int_{\phi_1}^{+\infty} h(x)dx = 0.5 \tag{8d}$$

$$\int_{-\infty}^{+\infty} x.h(x)dx = \phi_0 \tag{8e}$$

Representing the value obtained from the finest grid by ϕ_1, the confidence interval (CI) of the numerical uncertainty evaluation process is 95% between the bounds $y_b = \phi_1 - u$ and $y_t = \phi_1 + u$. The bounds are in equal distance from the ϕ_1 and, ϕ_1 represents the median point which means the probability of getting a higher or lower value from the median value is equal, as expressed in Eqs. (8c) and (8d), respectively. In similar mesh refinement applications in CFD, generally it is seen that the output response tending to increase or decrease as the grid is refined. This tendency can be tracked by the trend of the Richardson extrapolation function. If the function shows a concave behaviour, the output response tends to decrease as the mesh is refined; if it shows a convex behaviour, then the output tends to increase as the mesh is refined. It is desired to have a PDF which behaves like the convexity of Richardson extrapolation. Because of that, the expected value of the discrezation uncertainty h(x) is assumed as ϕ_0 in the last hypothesis adopted. This is not the exact usage of ϕ_0, its actual representation is to the idea

of having a infinite mesh, but here it is used to state which value should be expected. All the assumptions are given below. Further explanation is given by [2].

3 TEST CASE

In order to investigate the combined uncertainty in the estimation of dynamic cavitation inception, NACA 66 foil which is studied experimentally by [1] and other authors, is chosen due to its popularity and its affinity to marine propeller design, and wide availability of experimental and reference numerical data [55–61].

3.1 Geometry

A two-dimensional cambered foil of the NACA 66 series, has relative maximum thickness of 12% at the chordwise ordinate x/c=0.45 from the leading edge. The relative maximum camber is 2% and is located at x/c=0.50 from the leading edge. The chord length c is 0.150 m. The flow is considered to be two-dimensional. Further description of the experimental set up is given in [1].

3.2 Computational Domain, Initial and Boundary Conditions

The geometry of the domain and the boundary conditions of this study are shown in Figure 6. A rectangular domain is used for the simulation in order to mimic the test section of the cavitation tunnel used in the source experimental study. The domain extends 0.4125 m upstream and 1.050 m downstream. Velocity inlet boundary condition is used and fixed pressure is prescribed at the outlet. Symmetry boundary conditions are selected for the top and the bottom parts of the domain and a no-slip wall boundary condition is assigned to the foil. Inflow velocity is given as 5.33 m/s, leading to the same Reynolds number as in the reference study [1].

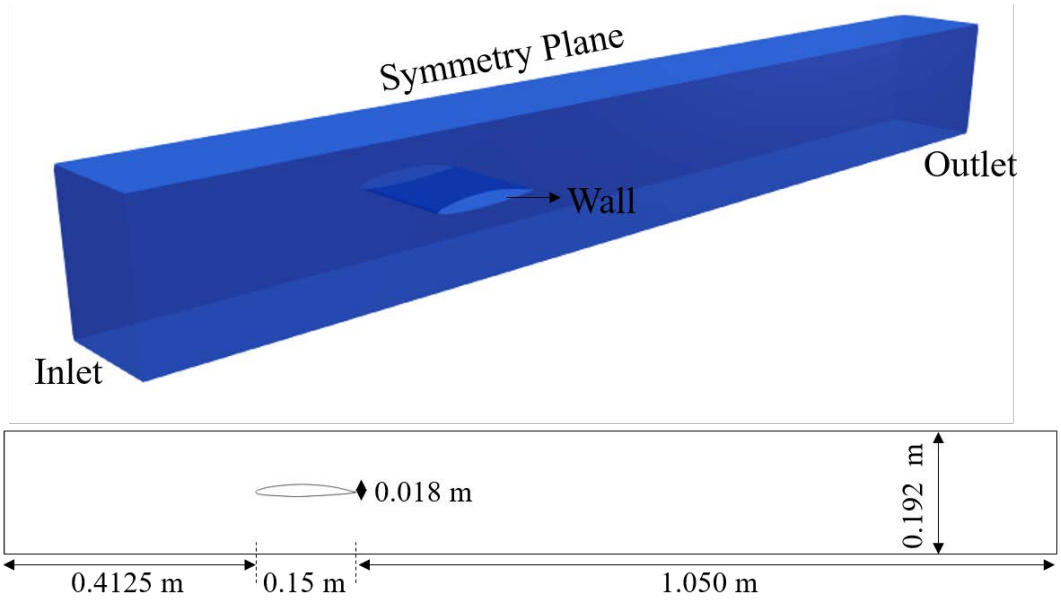

Figure 6: Domain geometry and boundary conditions.

3.3 Grid Topology

Grids are block-structured and each block in each direction experience the same coarsening factor. h represents the typical cell size and it is equal to $1/\sqrt[2]{N}$ with N designating the total number of cells. Thus, the relative step size between the coarser grids $i \geq 1$ and the finest grid $i = 1$ becomes

$$\frac{h_i}{h_1} = \sqrt[2]{N_1/N_i}. \tag{9}$$

Mesh G1 (the coarsest mesh, out of eight refined meshes studied in the framework of this study) topology along the whole computational domain and different section views of leading edge area from other refined grids are shown in Figure 7 Also, names and the characteristics of the grids are given in Table 1.

Table 1: Characteristics of the grid series used in the present study.

Mesh Name	**Refinement Ratio** (f)	**Cell Count**	**Relative step size** (h_i/h_1)
G1	0.7	45,184	2.4434
G2	0.8	55,476	2.2447
G3	0.9	79,156	1.9459
G4	1.0	91,632	1.7389
G5	1.2	136,620	1.4241
G6	1.4	171,088	1.3236
G7	1.6	227,680	1.1081
G8	1.8	269,808	1.0000

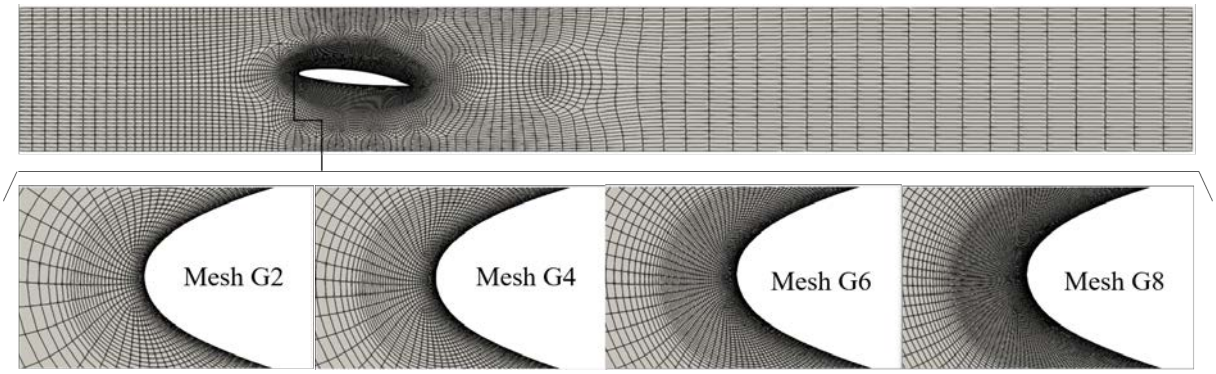

Figure 7: View of the grid G1 topology of complete computational domain (top); and views of leading edge area from different refined grids (bottom)

3.4 Numerical Setup

Simulations are carried out by using the multi-phase viscous flow solver ReFRESCO version 2023.1.0. The code was first developed within the VIRTUE EU Project [62] and is still being developed by specialists at MARIN and many participants all around the world.

Because of the need to achieve tight iterative convergence tolerances in order to facilitate accurate uncertainty quantification, careful choices of the discretization schemes and solver settings are made. The momentum conservation equations are solved by using PETSc-GMRES

solver with JACOBI preconditioner and discretised using the LIMITED QUICK scheme for the convective flux discretization. For pressure equation, PETSc-CG solver with BJACOBI preconditioner is used. Turbulence is modelled by using Scale-Adaptive-Simulation Model (KSKL-Standard) turbulence model and turbulent transport equations are solved by PETSc-GMRES solver with BJACOBI preconditioner. Cavitation modeling is carried out by using Schnerr-Sauer cavitation model [63].

At the beginning of the simulation, the initial pressure is given as -250 kPa in order to prevent the presence of cavitation. After the steady non-cavitating flow has been established, the saturated vapour pressure value is gradually adjusted following a Hermite polynomial to reach to the desired cavitation number. Foil angle of attack obtained by deforming the baseline grid that has been generated at a zero incidence angle. In this approach, the cells in direct vicinity to the foil surface are fixed to the solid body and those further away are deformed using radial basis functions. This approach avoids the need to generate a new grid for each condition, speeding up the computations and ensuring that the results remain consistent within the complete matrix of simulations. Residual convergence criteria are set to $1x10^{-5}$ in L_∞ norm for all transport equations. Additional key parameters of simulation setup are listed in Table 2.

Table 2: Key parameters of simulation setup

Parameter	**Value**	**Unit**
Dynamic viscosity, μ	$9.9938x10^{-4}$	kg (m s)$^{-1}$
Water density, ρ_w	1000	kg m^{-3}
Inflow speed, U_∞	5.33	m s $^{-1}$
Reynolds number, Re	8 x 10^5	-
Cavitation number, σ	1.4719 to 1.6269	-
Angle of attack, α	5.70 to 6.30	deg
Vapour density, ρ_v	0.024	kg^2 m^{-3}
Bubble kinematic viscosity, ν_B	1.02·10^{-5}	m^{2}s^{-1}

3.5 Input and Output Variables

The angle of attack (Aoa) is the angle between the chord line and the relative flow direction. An increase in angle of attack increases both the lift and drag forces up to the stall angle. The cavitation number (σ) is a non-dimensional parameter describing how prone a particular flow is to cavitation. It is calculated by using a reference pressure (p), saturated vapor pressure (p_v), density of fluid, and velocity of flow:

$$\sigma = \frac{p - p_v}{\frac{1}{2}\rho_w U_\infty^2}. \tag{10}$$

The lower the cavitation number, the higher the probability of cavitation. In this study, velocity of the flow, density and reference pressure are kept constant. Saturation pressure values in each case are changed to achieve the desired cavitation number.

The lift coefficient (C_L) is a non-dimensional quantity that gives the relation of the lift force generated by a lifting surface to the density of fluid, flow velocity and the reference area. In this study, the lift force is considered as the force generated by the foil in the positive y-direction

(F_Y) and is calculated as

$$C_L = \frac{F_Y}{0.5\rho U_\infty^2 cs}. \tag{11}$$

In fluid dynamics, the drag coefficient (C_D) is a dimensionless quantity used to quantify the drag or resistance generated by an object in a fluid environment. In this study, drag force is considered as the force generated by the foil in the x-direction (F_X). It is computed according to

$$C_D = \frac{F_X}{0.5\rho U_\infty^2 cs}. \tag{12}$$

The cavitation length (L_{cav}) is computed by finding the minimum and maximum extents of the stable sheet cavity present on the hydrofoil. In order to make the results more consistent and representative of what would be observed visually during the experiments, only cells with vapour volume fraction higher than 0.25 are taken into account in the computation. The obtained value is then non-dimensionalized by the chord length, leading to

$$L_{\text{cav}} = \frac{x_{\text{cav max}} - x_{\text{cav min}}}{c}. \tag{13}$$

Total cavitation volume (V_{cav}) is obtained by performing a finite weighted sum of all the cells filled with vapour. The final result is made non-dimensional by using the span length and square of the chord length,

$$V_{\text{cav}} = \frac{\sum_{\text{iCell}=0}^{N_{\text{cells}}} V_{\text{iCell}} \alpha_{\text{iCell}}}{sc^2}. \tag{14}$$

4 RESULTS

4.1 Validation

In the first stage of this study, CFD simulations with and without cavitation were made in order to compare the results with the experimental results given in the study of Leroux et al. [1].

Interestingly, for high cavitation numbers, corresponding to little cavitation, the most pronounced differences may be seen. This is likely indicative of discrepancies between the numerical and experimental set ups that cannot be accurately discerned from the description of the experiments provided in [1] and [64]. At the same time, the trends in the analysed quantities, especially drag and cavity length, match the experiments very well. The magnitude of the lift coefficient also matches the measurements more closely at low σ values with a relative error of under 3%.

Iterative convergence of the SIMPLE algorithm inside each CFD time step is necessary for UQ applications in CFD in order to guarantee that true sensitivities and not numerical noise are being analysed inside the batch of simulations used as UQ inputs. One of the most influential parameters in achieving good iterative convergence is the Courant number. Due to use of an implicit time scheme, having a maximum Courant number approximately 10 has been found to be acceptable. Usually, approximately 80 outer loops were performed within each time step with a hard maximum of 100 imposed in order to reduce the risk of the simulation getting stuck at a time step that is particularly difficult to converge. The residuals for a case of intermediate refined mesh (G4) is shown in Figure 8. Two normalization types which are L_2 and L_∞ are chosen to check convergence of the simulations. As can be seen, after approximately 3000 time steps, corresponding to the establishing of a fully-developed flow, the residuals converge in a repetitive fashion.

Although the chosen experimental condition may be classified as steady sheet cavitation, in reality small oscillations of the trailing edge of the cavity were observed in the computations. In order to guarantee statistical convergence of the results, 25,000 time steps were used in each computation, with the first 1,000 time steps being discarded from the analysis due to start up effects. Time histories of the considered output quantities obtained from an example simulation are depicted in Figure 9.

A python module called pyTST which implements the ”Transient Scanning Technique” presented in [65–67] is used to check whether the selected number of time step is sufficient or not. pyTST module allows to detect transient portion of a signal and measure the statistical uncertainty with that portion removed [68].

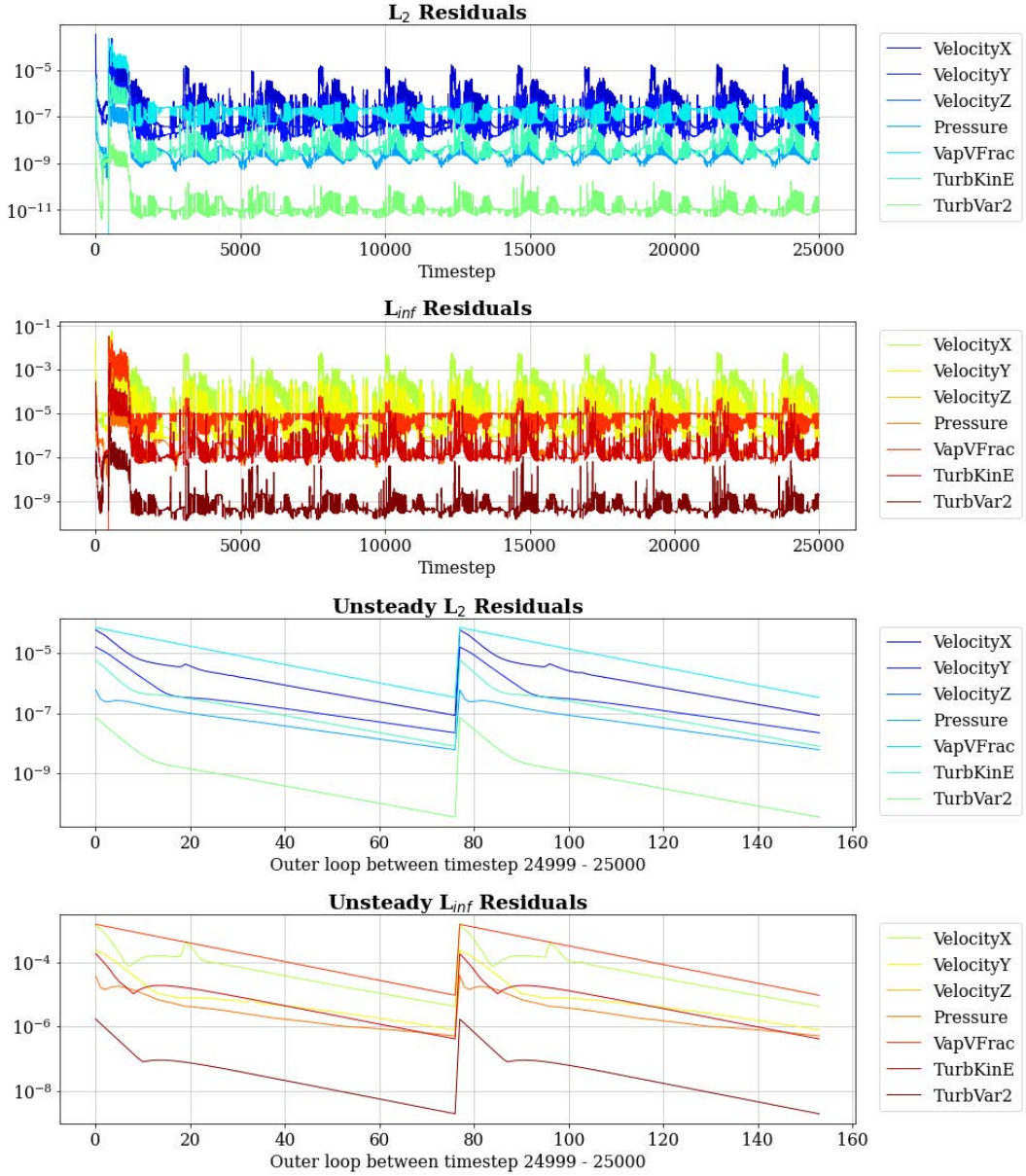

Figure 8: L_2 and L_∞ residuals of a case for intermediate refined mesh (G4) for input parameters as $\sigma = 1.6102$ and $\alpha = 6.0065°$.

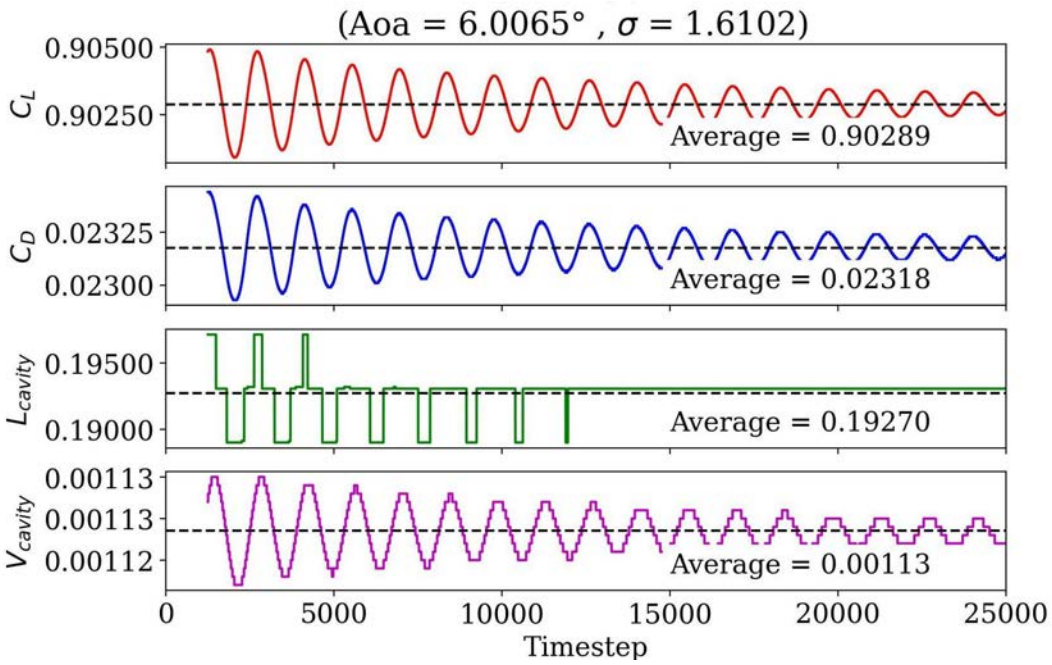

Figure 9: Convergence of the output parameters for intermediate refined mesh (G4) for input parameters as $\sigma = 1.6102$ and $\alpha = 6.0065°$.

4.2 Uncertainty quantification

Uncertainties are quantified for 8 grids of varying densities, using 25 sampling points. Key results of the analysis are the discretization uncertainties and Sobol. They are shown in Figure 10. The h_i/h_1 values given on the x-axis indicate the relative grid size, defined as per the work of [54]. In this study, $h_i/h_1 = 1$ refers to the finest mesh and $h_i/h_1 = 2.4434$ to the coarsest mesh. In the left-hand side figures, the discretization uncertainties, which do not take into account the parameter uncertainties and use the expected values of the input parameters, are represented with continuous error bars. $h_i/h_1 = 0$ represents the extrapolated value corresponding to infinite grid refinement, in which case the value read on the y-axis will be the expected value of the output parameter. The error bars given for each grid show the different percentage between the value to be reached on the infinitely refined grid (expected value) and the value in that grid. The values on or below of the error bars represent the uncertainty value which is calculated by multiplying the error value with a safety factor for the corresponding grid. The expected behavior in such a plot is that the error bars get shorter as the refinement in the grid increases. Such behavior indicates that discretization-induced errors in the simulation results decrease as the grid is refined. The value in the left-below side of the figure (value on the the bottom dashed line) represent the combined uncertainty value for the corresponding output parameter. Combined uncertainty value is the sum of each input uncertainties and discretization uncertainty. In the right-hand side figures, the colored bars represent the Sobol indices of the input parameters for each relative grid size. The bars in the left part of the plot correspond to the Sobol indices obtained by the combined uncertainty approach containing both the parameter and grid uncertainty. Colored lines represent the total-order Sobol indices. Also, total-order Sobol indices of the combined approach are shown with markers.

In the two plots on the top row for the C_L parameter, the magnitude of the discretization uncertainty does not decrease further with grid refinement providing results with 0.0% - 0.1% uncertainty margin, i.e. very close to the expected value for the C_L parameter. This shows

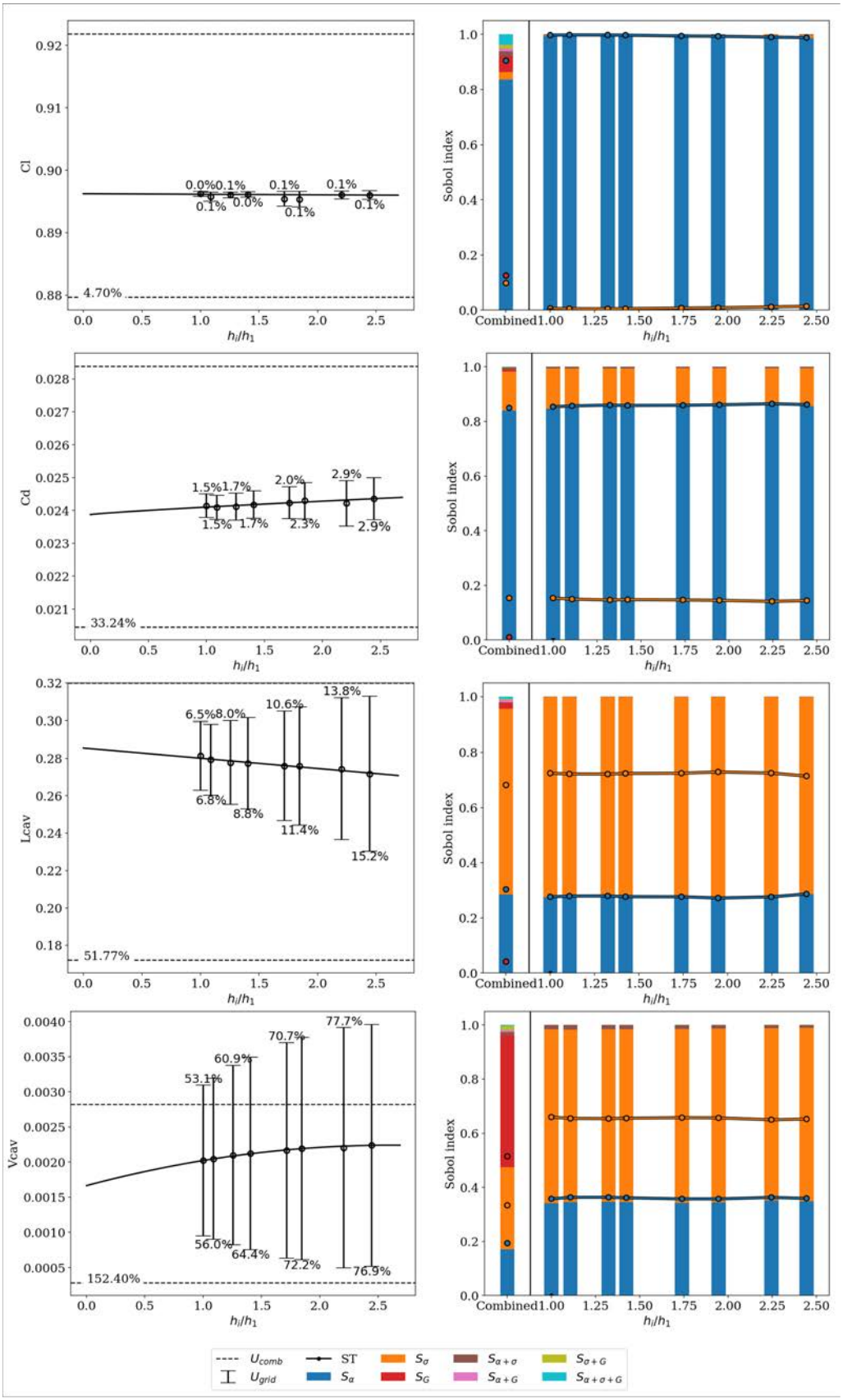

Figure 10: Comparison between parameter uncertainty and discretization uncertainty U_{grid}. Sobol indices are shown for each grid and for the combined uncertainty (right). Total-effect Sobol indices are represented by lines.

that even the coarsest grid is sufficient for the determination of this parameter. The combined uncertainty for C_L parameter is 4.70%. The greater effect on this value comes from the input parameter uncertainties, especially from the angle of attack S_α. In the combined uncertainty analysis, the individual effect of the S_α index (angle of attack) decreased from 0.99 to 0.84, while ST1, which expresses the total effect of the first parameter including its interaction with the second and third parameters, decreased to 0.90. Also, it can be observed that the effect of the cavitation number parameter, which almost cannot be seen on parameter uncertainty bars, increases noticeably here. In addition, by looking at the red colored part of the combined uncertainty bar, namely the Sobol index (S_G) of the grid refinement parameter, it can be seen that the grid has more effect on C_L than the cavitation number. Although refinement ratio did not affect the accuracy of the results much (according to the grid-uncertainty bars of C_L), it is seen that it the changes the influence of input parameters on the results.

Looking at the left-hand side figure for the C_D parameter, it is seen that in the discretization uncertainty study, the four coarsest grids have a 2.9% uncertainty according to the expected value of C_D in the infinite refinement state of the fitted exponential curve. Although this uncertainty value is higher than the uncertainty in the C_L parameter, it is deemed acceptable for practical purposes, particularly in the light of the aforementioned likely discrepancies between the numerical and experimental set ups. When the grid refinement process is continued, the uncertainty level in the finest grid decreases to 1.5%, showing that if the grid is sufficiently refined, the expected value can be approached but far more cells would be required to drive the uncertainty to a magnitude comparable to that of the lift coefficient. In the parameter uncertainty results, it is seen that the individual Sobol index of the 1st parameter (S_α - angle of attack) is dominant over the second parameter (S_σ - cavitation number), but not as dominant as in the case of C_L. Also, the effect of the first parameter, including its interaction with the second parameter (ST1), represented by the blue line, appears to be slightly different from the individual effect. The same is true for the second input parameter. This shows that the input parameters do not have a significant interaction with each other in the calculation of the C_D coefficient, and that the angle of attack of the foil is the main factor affecting the drag coefficient by itself. In the combined parameter uncertainty part, it is seen that the grid uncertainty (red) has a shorter bar than in the case of the lift coefficient. In other words, application of grid refinement does not significantly affect the results. Furthermore, the inclusion of grid uncertainty in the analysis reduces the effect of the first input parameter on C_D, while increasing that of the second input parameter, but only slightly.

In the discretization uncertainty figure presented for the cavitation length, it is seen that the grid refinement process has more effect on the cavitation length parameter than the previous two output parameters. This inference has been made considering that the uncertainty value difference between the coarsest grid and the finest grid is around 8% for the L_{cav} value. The fact that the grid refinement process approaches the actual value of the output parameter in each refinement is exactly as expected from this process. Since the fitted exponential curve and the length of error bars decrease regularly as the relative step size (h_i/h_1) ratio decreases, it seems possible to obtain results much closer to the expected value for the L_{cav} parameter by continuing the grid refinement process. It is seen that the grid uncertainty parameter has a very low effect on the output parameters compared to the other two input parameters. This is an important takeaway, as although the grid uncertainty is quite large here (6.5%-15.2%), it is far less important than the uncertainties over the angle of attack and cavitation number.

Looking at the discretization uncertainty figure for the V_{cav} parameter, it is seen that as the grid is refined, the discretization uncertainty bars get shorter, that is, the V_{cav} value approaches

the expected value. It may also be seen that the Sobol index corresponding to the discretization effect is noticeably higher for the cavitation volume than for the other output parameters. This can be understood from the fact that the uncertainty values have approximately 24% difference between the finest grid and the coarsest grid. The high levels of discretization uncertainty also indicate that further refinement would be necessary in order to arrive at a set of converged values and more reliable uncertainty estimates. In the parameter uncertainty part of the right-hand side figure for V_{cav}, it is seen that the individual effects of the input parameters are close to each other. However, as it is in L_{cav}, the cavitation number is the more influential than the angle of attack. In the combined parameter uncertainty results, it is seen that the grid uncertainty (red bar) has the greatest effect on the outputs. Also, the total-effect Sobol indices of the combined study show that the discretization uncertainty has the highest influence on V_{cav} uncertainty, with ST3 = 0.52, followed by the cavitation number with ST2 = 0.34 and angle of attack ST1 with 0.19. To reduce the combined uncertainty, a much finer mesh is necessary.

As a summary of the results presented in this study: the discretization uncertainty may be the dominant contributor to the output uncertainties for some parameters, but the input uncertainties also have a significant and relevant effect. Furthermore, in flows where turbulence intensity is high and cavitation is present, although the selected grid can accurately capture parameters such as C_L and C_D calculated by reading the forces, it may not be as successful in capturing unstable parameters such as L_{cav} and V_{cav} . In such cases, the combined uncertainty effect would be much more. But this can be reduced by refining the grid especially for the output parameter of Vcav.

5 CONCLUSIONS

This work presented the estimation of the combined effect of parameter and discretization uncertainties, showing the confidence interval and Sobol indices in CFD simulations of dynamic cavitation. Two uncertain input variables, the angle of attack and cavitation number, were chosen and evaluated on the example of a NACA66 hydrofoil. Also, in order to investigate the discretization uncertainty effect on the output parameters, grid uncertainty has been considered as the third input parameter. Although the simulations were carried out in 2D, the computational cost of performing a large number of computations on each grid refinement level was a significant hindrance and highlights the difficulty in applying UQ to CFD simulations. As a consequence, a surrogate model approach was employed to allow the Sobol analysis to be carried out using fewer computational results. It was observed that, for output parameters such as drag coefficient (C_D) and cavitation length (L_{cav}), the confidence intervals and Sobol indices were barely observed to change with varying grid refinement, showing a predominance of parameter uncertainties. For the lift coefficient (C_L), it was seen that the discretization uncertainty effect was greater than for C_D and V_{cav} , but still the parameter uncertainty was dominant over the discretization uncertainty. For the cavitation volume (V_{cav}), the reverse trend has been observed whereby the discretization uncertainty was dominant instead of the parameter uncertainty. However, parameter uncertainty still had a significant influence on this output parameter.

For future works, the presented analysis framework could be extended in order to develop a formulation for unsteady applications and include the effects of iterative uncertainty or time step uncertainty alongside the grid and input uncertainty quantification. Other parameters, such as coefficients related to turbulence or cavitation models, could be included to factor in additional degrees of the modelling uncertainties in addition to the grid and operating point conditions (angle of attack and cavitation number).

References

[1] Jean-Baptiste Leroux, Jacques André Astolfi, and Jean Yves Billard. An experimental study of unsteady partial cavitation. *J. Fluids Eng.*, 126(1):94–101, 2004.

[2] Eduardo Tadashi Katsuno, Artur K Lidtke, Bülent Düz, Douwe Rijpkema, João LD Dantas, and Guilherme Vaz. Estimating parameter and discretization uncertainties using a laminar–turbulent transition model. *Computers & Fluids*, 230:105129, 2021.

[3] Ralph C Smith. *Uncertainty quantification: theory, implementation, and applications*, volume 12. Siam, 2013.

[4] Timothy John Sullivan. *Introduction to uncertainty quantification*, volume 63. Springer, 2015.

[5] Chris Lacor, Cristian Dinescu, Charles Hirsch, and Sergey Smirnov. Implementation of intrusive polynomial chaos in cfd codes and application to 3d navier-stokes. *Uncertainty quantification in computational fluid dynamics*, pages 193–223, 2013.

[6] Dakota software training, uncertainty quantification. `https://dakota.sandia.gov/sites/default/files/training/DakotaTraining_UncertaintyQuantification.pdf`, 2016. Accessed: 2023–01-21.

[7] Cristian Dinescu, Sergey Smirnov, Charles Hirsch, and Chris Lacor. Assessment of intrusive and non-intrusive non-deterministic CFD methodologies based on polynomial chaos expansions. *International Journal of Engineering Systems Modelling and Simulation*, 2(1-2):87–98, 2010.

[8] Tyrone S Phillips and Christopher J Roy. A new extrapolation-based uncertainty estimator for computational fluid dynamics. *Journal of Verification, Validation and Uncertainty Quantification*, 1(4), 2016.

[9] Alessandra Cuneo, Alberto Traverso, and Shahrokh Shahpar. Comparative analysis of methodologies for uncertainty propagation and quantification. In *Turbo Expo: Power for Land, Sea, and Air*, volume 50800, page V02CT47A005. American Society of Mechanical Engineers, 2017.

[10] L. Gilli, D. Lathouwers, J.L. Kloosterman, T.H.J.J. van der Hagen, A.J. Koning, and D. Rochman. Uncertainty quantification for criticality problems using non-intrusive and adaptive polynomial chaos techniques. *Annals of Nuclear Energy*, 56:71–80, 2013.

[11] Jiju Antony. *Design of experiments for engineers and scientists*. Elsevier, 2014.

[12] Jon C Helton. Uncertainty and sensitivity analysis in the presence of stochastic and subjective uncertainty. *journal of statistical computation and simulation*, 57(1-4):3–76, 1997.

[13] D Robinson and C Atcitty. Comparison of quasi-and pseudo-monte carlo sampling for reliability and uncertainty analysis. In *40th Structures, Structural Dynamics, and Materials Conference and Exhibit*, page 1589, 1999.

[14] Nicholas Metropolis and Stanislaw Ulam. The monte carlo method. *Journal of the American statistical association*, 44(247):335–341, 1949.

[15] Michael D McKay, Richard J Beckman, and William J Conover. A comparison of three methods for selecting values of input variables in the analysis of output from a computer code. *Technometrics*, 42(1):55–61, 2000.

[16] Eduardo Saliby. Descriptive sampling: a better approach to monte carlo simulation. *Journal of the Operational Research Society*, 41(12):1133–1142, 1990.

[17] Felipe AC Viana. A tutorial on latin hypercube design of experiments. *Quality and reliability engineering international*, 32(5):1975–1985, 2016.

[18] John M Hammersley. Monte carlo methods for solving multivariable problems. *Annals of the New York Academy of Sciences*, 86(3):844–874, 1960.

[19] Jayant R Kalagnanam and Urmila M Diwekar. An efficient sampling technique for off-line quality control. *Technometrics*, 39(3):308–319, 1997.

[20] J-A Astolfi, J-B Leroux, P Dorange, J-Y Billard, F Deniset, and S De La Fuente. An experimental investigation of cavitation inception and development on a two-dimensional hydrofoil. *Journal of ship research*, 44(04):259–269, 2000.

[21] András Sobester, Alexander Forrester, and Andy Keane. *Engineering design via surrogate modelling: a practical guide*. John Wiley & Sons, 2008.

[22] Emiliano Torre, Stefano Marelli, Paul Embrechts, and Bruno Sudret. A general framework for data-driven uncertainty quantification under complex input dependencies using vine copulas. *Probabilistic Engineering Mechanics*, 55:1–16, 2019.

[23] Habib N Najm. Uncertainty quantification and polynomial chaos techniques in computational fluid dynamics. *Annual review of fluid mechanics*, 41:35–52, 2009.

[24] Richard P Dwight, Jeroen AS Witteveen, and Hester Bijl. *Adaptive uncertainty quantification for computational fluid dynamics*. Springer, 2013.

[25] Timothy Simpson, Vasilli Toropov, Vladimir Balabanov, and Felipe Viana. Design and analysis of computer experiments in multidisciplinary design optimization: a review of how far we have come-or not. In *12th AIAA/ISSMO multidisciplinary analysis and optimization conference*, page 5802, 2008.

[26] Ying Zhao, Wenxi Lu, and Chuanning Xiao. A kriging surrogate model coupled in simulation–optimization approach for identifying release history of groundwater sources. *Journal of Contaminant Hydrology*, 185:51–60, 2016.

[27] Francisco-Javier Granados-Ortiz, Carlos Perez Arroyo, Guillaume Puigt, Choi-Hong Lai, and Christophe Airiau. On the influence of uncertainty in computational simulations of a high-speed jet flow from an aircraft exhaust. *Computers & Fluids*, 180:139–158, 2019.

[28] Jerome H Friedman. Multivariate adaptive regression splines. *The annals of statistics*, 19(1):1–67, 1991.

[29] G Jekabsons. Varireg: a software tool for regression modelling using various modeling methods. *Riga Technical University*, 2010.

[30] David G Kleinbaum, Lawrence L Kupper, Azhar Nizam, and Eli S Rosenberg. *Applied regression analysis and other multivariable methods*. Cengage Learning, 2013.

[31] Wengang Zhang, Anthony TC Goh, and Yanmei Zhang. Multivariate adaptive regression splines application for multivariate geotechnical problems with big data. *Geotechnical and Geological Engineering*, 34:193–204, 2016.

[32] Kok Sung Won, Tapabrata Ray, and Kang Tai. A framework for optimization using approximate functions. In *The 2003 Congress on Evolutionary Computation, 2003. CEC'03.*, volume 3, pages 1520–1527. IEEE, 2003.

[33] Kok Sung Won and Tapabrata Ray. A framework for design optimization using surrogates. *Engineering optimization*, 37(7):685–703, 2005.

[34] Raj Mohan Singh, Bithin Datta, and Ashu Jain. Identification of unknown groundwater pollution sources using artificial neural networks. *Journal of water resources planning and management*, 130(6):506–514, 2004.

[35] P Lancaster and Kestutis Salkauskas. An introduction: curve and surface fitting. *Unpublished, Division of Applied Mathematics, University of Calgary*, 114, 1986.

[36] Piotr Breitkopf, Alain Rassineux, and Pierre Villon. An introduction to moving least squares meshfree methods. *Revue européenne des éléments finis*, 11(7-8):825–867, 2002.

[37] Dirk Roos, Thomas Most, JF Unger, and Johannes Will. Advanced surrogate models within the robustness evaluation. *Proc. Weimarer Optimierungs-und Stochastiktage*, 4:29–30, 2007.

[38] Benjamin Peherstorfer, Karen Willcox, and Max Gunzburger. Survey of multifidelity methods in uncertainty propagation, inference, and optimization. *Siam Review*, 60(3):550–591, 2018.

[39] Jie Zhang, Souma Chowdhury, and Achille Messac. An adaptive hybrid surrogate model. *Structural and Multidisciplinary Optimization*, 46:223–238, 2012.

[40] Koji Shimoyama and Akihiro Inoue. Uncertainty quantification by the nonintrusive polynomial chaos expansion with an adjustment strategy. *AIAA journal*, 54(10):3107–3116, 2016.

[41] Maliki Moustapha and Bruno Sudret. A two-stage surrogate modelling approach for the approximation of models with non-smooth outputs. 2019.

[42] Raymond Sedwick and Samuel Schweighart. Development and analysis of a high fidelity linearized j (2) model for satellite formation flying. In *AIAA space 2001 Conference and exposition*, page 4744, 2001.

[43] Sei-ichiro Sakata. Adaptive strategy for stochastic homogenization and multiscale stochastic stress analysis. In *Multiscale Modeling and Uncertainty Quantification of Materials and Structures: Proceedings of the IUTAM Symposium held at Santorini, Greece, September 9-11, 2013.*, pages 51–66. Springer, 2014.

[44] Ming-Hua Lin, John Gunnar Carlsson, Dongdong Ge, Jianming Shi, and Jung-Fa Tsai. A review of piecewise linearization methods. *Mathematical problems in Engineering*, 2013, 2013.

[45] X-Y Zhang, Mirjam N Trame, Lawrence J Lesko, and Stephan Schmidt. Sobol sensitivity analysis: a tool to guide the development and evaluation of systems pharmacology models. *CPT: pharmacometrics & systems pharmacology*, 4(2):69–79, 2015.

[46] Ilya M Sobol. Sensitivity analysis for non-linear mathematical models. *Math. Modeling Comput. Exp.*, 1:407–414, 1993.

[47] Andrea Saltelli, Stefano Tarantola, and KP-S Chan. A quantitative model-independent method for global sensitivity analysis of model output. *Technometrics*, 41(1):39–56, 1999.

[48] Toshimitsu Homma and Andrea Saltelli. Importance measures in global sensitivity analysis of nonlinear models. *Reliability Engineering & System Safety*, 52(1):1–17, 1996.

[49] Il'ya Meerovich Sobol'. Global sensitivity indices for the investigation of nonlinear mathematical models. *Matematicheskoe modelirovanie*, 17(9):43–52, 2005.

[50] Andrea Saltelli, Paola Annoni, Ivano Azzini, Francesca Campolongo, Marco Ratto, and Stefano Tarantola. Variance based sensitivity analysis of model output. design and estimator for the total sensitivity index. *Computer physics communications*, 181(2):259–270, 2010.

[51] V Gregory Weirs, James R Kamm, Laura P Swiler, Stefano Tarantola, Marco Ratto, Brian M Adams, William J Rider, and Michael S Eldred. Sensitivity analysis techniques applied to a system of hyperbolic conservation laws. *Reliability Engineering & System Safety*, 107:157–170, 2012.

[52] Jon Herman and Will Usher. Salib: An open-source python library for sensitivity analysis. *Journal of Open Source Software*, 2(9):97, 2017.

[53] Vaart AWvd. Asymptotic statistics. cambridge series in statistical and probabilistic mathematics, 1998.

[54] Luis Eça and Martin Hoekstra. A procedure for the estimation of the numerical uncertainty of cfd calculations based on grid refinement studies. *Journal of computational physics*, 262:104–130, 2014.

[55] Norman S Land. Characteristics of an naca 66, s-209 section hydrofoil at several depths. Technical report, 1943.

[56] Antoine Ducoin, Biao Huang, and Yin Lu Young. Numerical modeling of unsteady cavitating flows around a stationary hydrofoil. *International Journal of Rotating Machinery*, 2012, 2012.

[57] VH Hidalgo, XW Luo, X Escaler, J Ji, and A Aguinaga. Numerical investigation of unsteady cavitation around a naca 66 hydrofoil using openfoam. In *IOP Conference Series: Earth and Environmental Science*, volume 22, page 052013. IOP Publishing, 2014.

[58] Ryoichi S Amano, Mohammad Qandil, Tarek Elgammal, Ahmad Abbas, and Ahmad Abdelhadi. Predicting the cavitation phenomena over the hydrofoil: Cfd validation. In *AIAA Scitech 2019 Forum*, page 0783, 2019.

[59] Young T Shen and Richard Eppler. Wing sections for hydrofoils—part 2: Nonsymmetrical profiles. *Journal of ship research*, 25(03):191–200, 1981.

[60] TB Francis and J Katz. Observations on the development of a tip vortex on a rectangular hydrofoil. 1988.

[61] PE Dimotakis, HF Gaebler, HT Hamaguchi, DB Lang, and YT Shen. Two-dimensional naca 66 (mod) hydrofoil high speed water tunnel tests. 1987.

[62] Guilherme Vaz, Serge Toxopeus, and Samuel Holmes. Calculation of manoeuvring forces on submarines using two viscous-flow solvers. In *International Conference on Offshore Mechanics and Arctic Engineering*, volume 49149, pages 621–633, 2010.

[63] Günter H. Schnerr and Jürgen Sauer. Physical and Numerical Modeling of Unsteady Cavitation Dynamics. In *ICMF-2001, 4th International Conference on Multiphase Flow*, May 2001. event-place: New Orleans, Louisiana, United States.

[64] Jean-Baptiste Leroux, Olivier Coutier-Delgosha, and Jacques André Astolfi. A joint experimental and numerical study of mechanisms associated to instability of partial cavitation on two-dimensional hydrofoil. *Physics of fluids*, 17(5):052101, 2005.

[65] J Brouwer, J Tukker, M Van Rijsbergen, et al. Uncertainty analysis of finite length measurement signals. In *The 3rd International Conference on Advanced Model Measurement Technology for the EU Maritime Industry (AMT'13), Gdansk, Poland*, pages 260–274, 2013.

[66] Joris Brouwer, Jan Tukker, and Martijn van Rijsbergen. Uncertainty analysis and stationarity test of finite length time series signals. 09 2015.

[67] Joris Brouwer, Jan Tukker, Yvette Klinkenberg, and Martijn van Rijsbergen. Random uncertainty of statistical moments in testing: Mean. *Ocean Engineering*, 182:563–576, 2019.

[68] Sébastien Lemaire and Maarten Klapwijk. pytst, January 2021.